

## PAPER



Cite this: *Phys. Chem. Chem. Phys.*,  
2018, 20, 784

Received 2nd September 2017,  
Accepted 21st November 2017

DOI: 10.1039/c7cp06003c

rsc.li/pccp

## Filament dynamics in confined chemical gardens and in filiform corrosion

Fabian Brau,<sup>a</sup> Florence Haudin,<sup>a</sup> Stephanie Thouvenel-Romans,<sup>b</sup>  
Anne De Wit,<sup>a</sup> Oliver Steinbock,<sup>b</sup> Silvana S. S. Cardoso<sup>c</sup> and  
Julyan H. E. Cartwright<sup>d,e</sup>

Two reaction systems that are at first sight very different produce similar macroscopic filamentary product trails. The systems are chemical gardens confined to a Hele-Shaw cell and corroding metal plates that undergo filiform corrosion. We show that the two systems are in fact very much alike. Our experiments and analysis show that filament dynamics obey similar scaling laws in both instances: filament motion is nearly ballistic and fully self-avoiding, which creates self-trapping events.

### 1 Introduction

When maintained out of equilibrium, physico-chemical systems can spontaneously self-organize in a rich variety of complex spatiotemporal patterns.<sup>1</sup> Their study offers deep insights into many natural phenomena and even suggests paradigm shifting technologies. They also provide a broad range of fundamental challenges like, for example, characterizing the relations between their length and time scales to understand how microscopic mechanisms lead to macroscopic order. Classical examples of nonequilibrium chemical systems are the Belousov-Zhabotinsky and the chlorite-iodide-malonic acid reactions, which self-organize in propagating concentration pulses, rotating spiral waves, and stationary Turing structures.<sup>2</sup> Corrosion and precipitation reactions may appear to be the dynamical antipodes of these examples, as both rust and precipitates are often perceived as unstructured and random. However, it is well established that both processes can generate a plethora of highly ordered structures and rhythms. For instance, inorganic precipitation reactions can create periodic Liesegang rings and complex microstructures called biomorphs.<sup>3</sup> Corrosion processes can oscillate in time, generating wave pulses and even self-organizing spiral waves.<sup>4-7</sup>

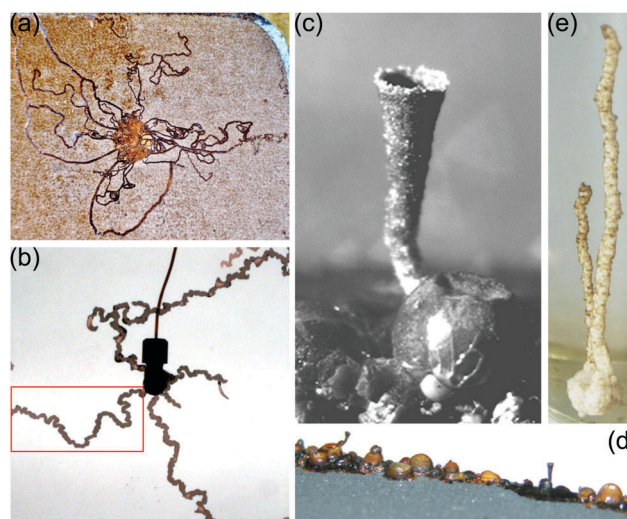


**Fig. 1** Two-dimensional filaments in spatially confined systems. (a) Filiform corrosion formed on a coated steel plate. Field of view:  $25 \times 20 \text{ mm}^2$ . (b) Filaments in confined geometry for aqueous solutions of cobalt chloride injected radially into sodium silicate obtained 15 s after injection began. Field of view:  $150 \times 150 \text{ mm}^2$ . The red rectangle highlights a filament analysed in Fig. 3. Details about experimental conditions are given in Section 2. Three-dimensional tubes in spatially unconfined systems. (c) Photo of a rust tube that spontaneously formed on a coated steel plate undergoing blistering corrosion. Field of view:  $2.0 \times 3.3 \text{ mm}^2$ . (d) Large view of the edge of the same steel plate showing numerous blisters and tubes. Field of view is  $3.3 \text{ cm}$  wide. (e) Precipitation tube in a 3D chemical garden formed by seeding a  $\text{MnCl}_2$  particle into a sodium silicate solution. Tube height is about  $3 \text{ cm}$ .

<sup>a</sup> Université libre de Bruxelles (ULB), Nonlinear Physical Chemistry Unit, Faculté des Sciences, CP-231, 1050 Brussels, Belgium. E-mail: fabian.brau@ulb.ac.be

<sup>b</sup> Department of Chemistry and Biochemistry, Florida State University, Tallahassee, FL 32306-4390, USA

<sup>c</sup> Department of Chemical Engineering and Biotechnology, University of Cambridge, Cambridge CB2 3RA, UK

<sup>d</sup> Instituto Andaluz de Ciencias de la Tierra, CSIC-Universidad de Granada, 18100 Armilla, Granada, Spain

<sup>e</sup> Instituto Carlos I de Física Teórica y Computacional, Universidad de Granada, 18071 Granada, Spain

In this work, we present a comparative study of trail-like reaction products formed during surface corrosion (Fig. 1(a)) and during the growth of a particular type of precipitation structure called chemical gardens (Fig. 1(b)). The former process is called filiform, or underfilm, corrosion and creates brown rust

filaments on the surface of – usually coated – steel, as well as similar corrosion on other metals such as aluminium. The latter creates, in its usual three-dimensional setting, hollow tubular structures (Fig. 1(e)).

Chemical gardens are plant-like mineral structures first described in the seventeenth century and popularly known from chemistry sets for children. They are classically grown in three-dimensional containers by placing a solid metal-salt seed into an alkaline silicate solution.<sup>8</sup> When the metal salt starts dissolving in the silicate solution (silicate is most often employed, but many other anions can also be used), a semi-permeable membrane forms by precipitation, across which water is pumped by osmosis from the silicate solution into the metal salt solution, further dissolving the salt. Above a given pressure, the membrane breaks. The dissolved metal salt solution, being generally less dense than the silicate solution, rises as a buoyant jet through the broken membrane and further precipitates in contact with the silicate solution, producing a collection of mineral forms that resemble a garden. The growth process of chemical gardens is thus driven by a complex coupling between osmotic, buoyancy and chemical precipitation reaction processes.<sup>9</sup> While classical chemical gardens are three dimensional and prone to form hollow tubes,<sup>10–13</sup> one can reduce the dimensionality of the system by using a Hele-Shaw cell, in which the reactants are confined between two flat plates spaced a small distance apart. Such confined chemical gardens produce an array of morphologies, among which filaments are prominent.<sup>14–16</sup>

The links between chemical gardens and certain types of corrosion are well established. Corrosion tubes are hollow tubular structures that have been noted and studied in iron corrosion under a variety of conditions. Fig. 1(c) and (d) show examples obtained under high-humidity conditions that give rise to blistering corrosion. These rust tubes are about 2 mm tall and form spontaneously from rust blisters on the corroding low-carbon steel plate.<sup>17</sup> For comparison, we also show a hollow precipitate tube in a typical chemical garden in Fig. 1(e). A recent review<sup>9</sup> has noted that both chemical gardens and tubular corrosion are examples of chemobronic systems which involve osmosis across a semipermeable membrane. Filiform corrosion – a spatially two-dimensional process – constitutes a special class of corrosion<sup>18</sup> (Fig. 1(a)). Filaments of corrosion products rove over a metallic substrate coated with a protective film; hence the alternative name “underfilm corrosion”. Filiform formation occurs on technologically relevant metals such as iron and aluminium and their alloys but also on less common substrates, for example magnesium<sup>19,20</sup> or uranium.<sup>21</sup> The nature of the film covering the metal surface can vary widely from sputtered tin, silver or gold to organic coatings such as enamels and lacquers.<sup>22</sup> Also the paperbacked side of aluminium paper has been reported to induce filiform corrosion.<sup>23</sup> Filiform corrosion has even been noted in the absence of any deliberately applied coating.<sup>24</sup> The formation of filiforms under these conditions is likely related to the presence of a thin water film on the metal surface and/or to a film of contaminants.<sup>25</sup>

Filiform corrosion is localized in the sense that only a minimal area of the surface corrodes at any given time, yet the trails of corrosion products can grow to tens of centimetres in length. The depth of the attack is shallow, generally some 5–15  $\mu\text{m}$ .<sup>26</sup> Filiform corrosion is thus not generally a problem in terms of loss of material strength, but rather one of aesthetics. Nevertheless, its economical impact is sizeable. Filiform corrosion is most virulent slightly above normal room temperature (20–40 °C) and for a relative humidity between 65–95% for steel and 70–95% for aluminium.<sup>19,22,27</sup> The filaments are initiated by contaminants<sup>28</sup> either under or above the protective film. Chlorides, sulfates, and carbonic acids are some obvious culprits; less obvious contaminants include petroleum-related substances and even tobacco fumes.<sup>23</sup>

As we have described, chemical gardens grow through a mechanism involving osmotic pressure differences across a membrane semipermeable to some ions. Likewise, it has long been known that “a significant feature of filiform corrosion is the osmotic action which supplies the anolyte present in the head of the filament” (Slabaugh and Grotheer<sup>19</sup>). To explain further the osmotic mechanism of filiform corrosion (see Fig. 2) we continue to quote Slabaugh and Grotheer, “the driving force of this type of corrosion is controlled by the osmotic action in the growing cell and the modification of the cell fluid which produces a significant boundary, B, between the blue head and the rust filament. Starting at A, the concentration of cell fluid is very high; hence the osmotic rate is high, because  $P_1$  is much greater than  $P_2$ . The resulting osmotic pressure is sufficient to disengage the film from the metal and form a cell. As the cell grows, both normal to the surface of the metal and laterally, the cell fluid becomes diluted by additional moisture entering the cell through osmosis. As the osmotic rate diminishes, chemical oxidation converts iron(II) to iron(III). Because of the presence of sufficient hydroxyl ions and the greatly reduced solubility of ferric salts compared to ferrous salts, the iron is precipitated at B as a hydrated ferric oxide. This abrupt reduction in the concentration of the cell solution causes an immediate reversal in the vapor pressure differential, with  $P_2$  now exceeding  $P_1$ . Beyond B the osmosis will be reversed by a transfer of moisture

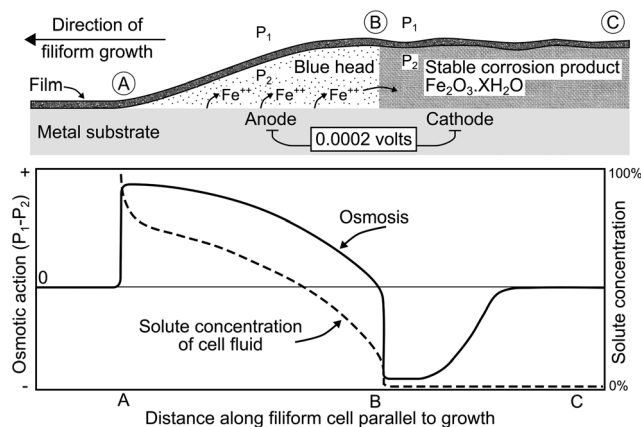


Fig. 2 Osmotic and electrochemical action in filiform corrosion. Adapted from Slabaugh and Grotheer.<sup>19</sup>

from the cell to the atmosphere. The contents of the filament at C are relatively dry, stable corrosion product." Slabaugh and Grotheer<sup>19</sup> suggest that the semipermeable membrane across which osmosis occurs is the film above the head of the filament. However, later work by Ruggeri and Beck<sup>20</sup> shows that the semipermeability of the tail (*i.e.*, the part labelled B to C in Fig. 2) may be key. Ruggeri and Beck cut and sealed the tails of filiforms and showed that in that case growth ceased. For both chemical gardens filaments and corrosion filiforms, it should be noted that for osmosis to operate, there should be the solvent, water, on each side of a semipermeable membrane that impedes the passage of some solute, whether determined by size or electric charge. This necessity for liquid water coincides with the high humidity under which filiform corrosion operates, such that there should be at least a thin film of liquid water on the outer side of the fluid cell.

Here we compare the dynamics of both filiform corrosion and filaments grown in confined chemical gardens. Both immediate phenomena occur under quasi-two dimensional conditions, *i.e.*, as effects in thin layers, and involve a localized, propagating reaction zone that creates a permanent reactant trail. Our study reveals non-trivial differences but also unexpected similarities that have not been acknowledged in the literature.

## 2 Materials and methods

### 2.1 Confined chemical gardens

The growth of chemical gardens is confined using a Hele-Shaw cell consisting of two transparent acrylate plates of size 215 mm × 215 mm × 8 mm separated by a gap of 0.5 mm. The metal salt solution is prepared by the dissolution in distilled water of cobalt chloride hexahydrate CoCl<sub>2</sub>·6H<sub>2</sub>O salt (Sigma Aldrich). The sodium silicate solution is obtained by dilution of a commercial solution of concentration 6.25 M with respect to silica SiO<sub>2</sub> (Sigma Aldrich).

The cell initially filled with a sodium silicate solution is placed horizontally on top of a light table providing a diffuse light. The metal salt is injected radially through a hole in the centre of the lower plate. The injection device comprises a syringe pump and a capillary tube, linked from one side to the syringe *via* a Luer lock connector. From the other side, a connector links the tube to the cell with no contact between the two fluids before injection starts at a flow rate,  $Q = 0.11 \text{ mL s}^{-1}$ , imposed by the syringe pump. The dynamics is recorded from above using a CMOS camera (either an Allied or a Pixelink digital camera).

### 2.2 Filiform corrosion

All experiments on filiform corrosion are carried out on low carbon steel plates (C1018, McMaster-Carr). The rectangular samples are sandblasted to remove contaminants (*e.g.*, grease from handling the metal) and grooves from the surface. Deionized water is then used to rinse the surface clean of metal particles, followed by an acetone rinse to dry the sample. To initiate the corrosion process and to control the location of the filiform

growth, the surface is exposed locally to 7  $\mu\text{L}$  aliquots of sodium chloride solution (8.6 mM) spaced at generous distances. The drops of solution are allowed to air dry for two hours prior to coating. The corrosion experiments are performed on samples covered by an acrylic coating. For this purpose, the steel plates are sprayed with crystal clear 1301 (Krylon), an organic lacquer of commercial grade with a formulation of 20% acryloid B-66 in toluene and ethyl methacrylate resin. The thickness of the dry film is varied by increasing the number of applied layers. A drying period of ten minutes is observed between applications. The resulting samples are set to cure under ambient conditions for 12 hours.

The corrosion process occurs at high relative humidity and slightly elevated temperature. To maintain these conditions, the samples are kept in individual sealed containers at 38 °C. Each container holds 30 mL of nitric acid solution (1 M). This solution is not in direct contact with the samples but establishes a corrosive environment and sets the relative humidity to a constant value of 80% (as verified by hygrometer measurements). The samples remain under these conditions for 45 to 70 days. After this time, numerous corrosion trails have formed that do not further change macroscopically under ambient conditions.

For the characterization of the samples, we employ an optical microscope (Intel QX-2) and a CCD camera (COHU 2100 RS-170). Surface height variations are analysed using a profilometer (P15, KLA-Tencor) and a conical stylus with a cone angle of 90° and a radius of 0.25  $\mu\text{m}$ . The profilometer was also used to measure the height of the dried acrylic coatings.

## 3 Filaments in confined chemical gardens

Depending on the concentration of the reactants, a rich variety of patterns are observed during the growth of chemical gardens in confined geometries.<sup>14–16</sup> When both concentrations are sufficiently large ( $[\text{CoCl}_2] \gtrsim 0.6 \text{ M}$  and  $[\text{Na}_2\text{SiO}_3] \gtrsim 3 \text{ M}$ ), filaments are produced as shown in Fig. 1(b).

In order to study their erratic growth, we perform image analysis. Each filament track is binarized and subsequently skeletonized as shown in Fig. 3(a). The variation of width,  $W(s)$ , along the filament is measured from the binarized track, see Fig. 3(b). The averaged width,  $\langle W \rangle$ , is then computed together with its standard deviation. The skeleton defines a parametrized trajectory for the filament:  $(x(s), y(s))$  where  $s$  is the arclength. The local curvature of the filament,  $\kappa(s)$ , is then computed from this parametric curve using

$$\kappa(s) = \frac{x'y'' - y'x''}{(x'^2 + y'^2)^{3/2}}, \quad (1)$$

where prime indicates a derivative with respect to  $s$ . Fig. 3(c) shows the variation of  $\kappa$  for one filament. The curvature fluctuates around a value of zero corresponding to a displacement along a straight line. As shown below, the peak of the curvature distribution is indeed located around  $\kappa = 0$  (see Fig. 4(b)).

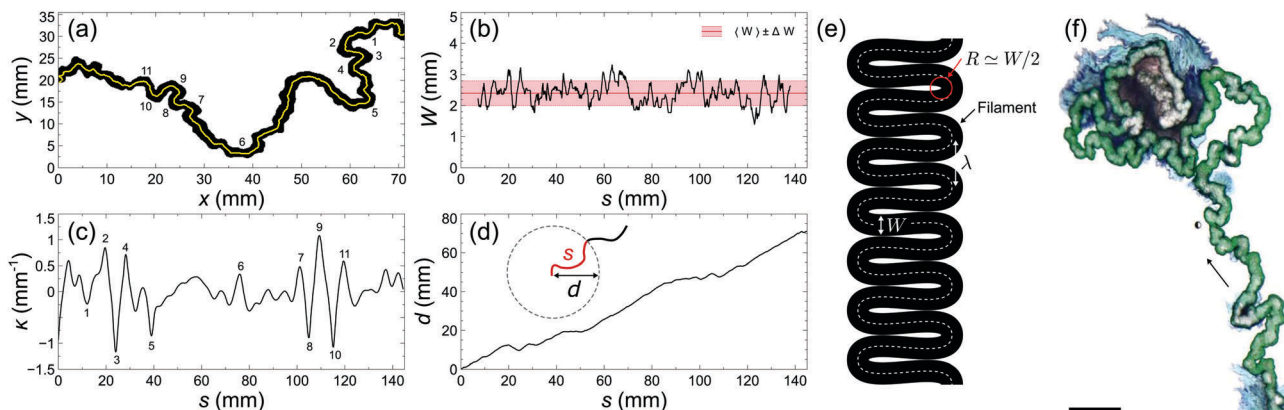


**Fig. 3** Confined chemical gardens. (a) Binarized track of a single filament shown in Fig. 1(b) (finite width) and its skeletonization (1 pixel width) used for the analysis. The numbers written along the filament indicate noticeable regions of relatively large local curvature. Ten additional filaments are used to perform the analysis displayed in Fig. 4. (b) Width of the same filament as a function of its arclength  $s$ . The average and standard deviation are:  $\langle W \rangle \pm \Delta W = (2.4 \pm 0.4)$  mm. (c) Curvature  $\kappa$  as a function of  $s$ . The numbers written along the curve refer to the regions of high local curvature shown in panel (a). (d) Euclidean distance,  $d$ , travelled by the filament as a function of  $s$ ; see the schematic in the inset. (e) Schematics of a filament of constant width  $W$  characterized by the largest possible local curvature  $\kappa_{\max} = 1/R = 2/W$  and the smallest possible wavelength  $\lambda = 2W$  due to self-contact. (f) Example of self-trapping during the growth of a chemical garden filament obtained by injecting a cobalt chloride solution (0.45 M) into a sodium silicate solution (6.25 M) at a flow rate  $Q = 0.11 \text{ mL s}^{-1}$ .<sup>16</sup> The arrow indicates the growth direction. Scale bar represents 1 cm.

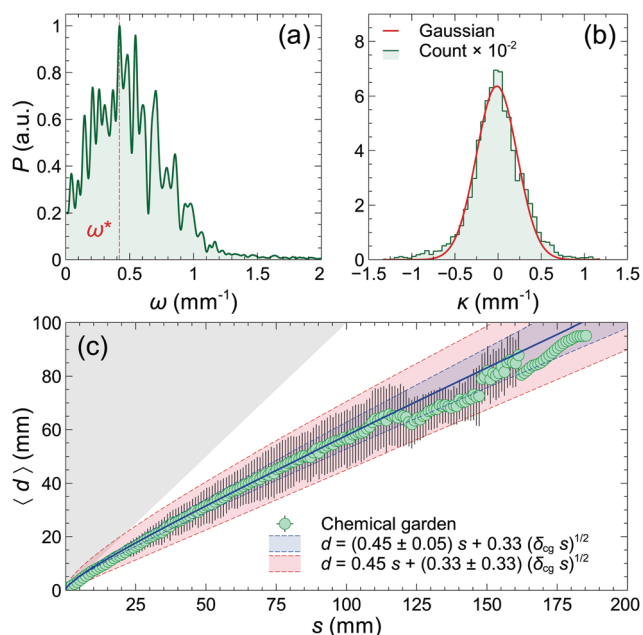


**Fig. 4** Confined chemical gardens: analysis of erratic directional changes along filament trajectories. (a) Normalized power spectrum of the curvature data of 11 filament trajectories. The preferred wavenumber,  $\omega^* = 0.42 \text{ mm}^{-1}$ , is also indicated. (b) Histogram of discrete values for the same data set together with a Gaussian fit. (c) Average Euclidean distance,  $\langle d \rangle$ , travelled by the 11 filaments as a function of their arclength  $s$ . The shaded area indicates a forbidden region where  $d > s$ .

The absolute value of the curvature is also bounded from above ( $|\kappa| \lesssim 1.15 \text{ mm}^{-1}$  in this example). This upper bound is related to the finite width of the filament. The largest curvature occurs when there is self-contact in a meander ( $|\kappa(s)| \lesssim 2/W(s)$ , see Fig. 3(e)). The parametrized trajectory allows one also to compute the Euclidean distance,  $d(s) = (x^2(s) + y^2(s))^{1/2}$ , travelled

during the filament growth as a function of its arclength  $s$ , as shown in Fig. 3(d). The Euclidean distance  $d(s)$  corresponds thus to the length of the straight line joining the starting point of the filament  $(x(0), y(0)) = (0, 0)$  to the point  $(x(s), y(s))$ .

The variations of those quantities ( $W$ ,  $\kappa$ , and  $d$ ) as a function of  $s$  have been obtained for eleven filaments. The evolution of the curvature  $\kappa$  along the filaments is similar to that shown in Fig. 3(c): its value fluctuates without a distinct pattern. A Fourier analysis of the data is therefore used to investigate the periodicity of  $\kappa(s)$  (see Appendix A). In Fig. 4(a), the power spectrum for all eleven filaments analysed is plotted as a function of wavenumber  $\omega$ . Significant amplitudes of the power are spread in the region  $\omega < \omega_c \simeq 1 \text{ mm}^{-1}$  with a preferred value,  $\omega^*$ , around  $0.4 \text{ mm}^{-1}$ . This cut-off indicates that the filaments are meandering with wavelengths larger than  $\lambda = 2\pi/\omega_c \simeq 6.3 \text{ mm}$ . In other words, most of the curvature data are located close to the origin and drop rapidly to zero for values larger than about  $1 \text{ mm}^{-1}$ . This cut-off value indicates that most turns made by the filaments occur around circles with radii  $R$  greater than  $1 \text{ mm}$ . This lower bound originates again from the finite width of the filaments, since self-contact limits the size of the meanders: for a filament of constant width  $\kappa_{\max} = 2/W$ , see Fig. 3(e). The averaged width of all filaments is found to be

$$\langle W_T \rangle \pm \Delta W_T = (2.3 \pm 0.5) \text{ mm}, \quad (2)$$

leading to  $\kappa_{\max} \sim 2/(\langle W_T \rangle - \Delta W_T) \simeq 1.1 \text{ mm}^{-1}$  in agreement with the cut-off obtained in Fig. 4(a).

Additional insights into the meandering motion of filaments can be obtained from a statistical analysis of curvature data. In Fig. 4(b), these data are presented in the form of a histogram. The continuous values of the curvatures are grouped in discrete bins. The shape of the histogram is essentially symmetric with

respect to zero. Indeed, the data can be well fitted by a Gaussian distribution

$$f(\kappa; \kappa_0, \sigma) = A e^{-\frac{(\kappa - \kappa_0)^2}{2\sigma^2}}, \quad (3)$$

with  $\sigma = 0.24 \text{ mm}^{-1}$  and  $\kappa_0 = -0.01 \text{ mm}^{-1}$  ( $A = 636$ ). The small value of  $\kappa_0$  confirms that the filament motion does not break chirality (*i.e.* left-right symmetry).

Fig. 4(c) shows a plot of the average Euclidean distance,  $\langle d \rangle$ , measured from the starting point of the filament trail (near the injection point) as a function of the filament arclength  $s$ . More precisely,  $\langle d \rangle$  is the average of all values of  $d$  corresponding to an arclength in the range  $[(n - 1)\Delta s, n\Delta s]$ , where  $\Delta s$  is some discrete increment (chosen here as  $0.5 \text{ mm} \simeq W/4$ ) and  $n \in [1, N]$ . The results are not sensitive to the precise value of  $\Delta s$ .  $N$  is the smallest integer larger than  $s_{\text{max}}/\Delta s$  where  $s_{\text{max}}$  is the maximum value of  $s$  for all filaments. Therefore, the data abscissae are equal to  $n\Delta s/2$  with a constant error equal to  $\pm\Delta s/2$  whereas the data ordinates are equal to  $\langle d \rangle$  with a variable error equal to the standard deviation of  $\langle d \rangle$ . The relationship between  $d$  and  $s$  can be described by a scaling approach developed in Section 5.

## 4 Filiform corrosion

Fig. 5 shows typical examples of the corrosion produced on low carbon steel plates. In each panel, the central region is a macroscopically featureless spot of corroded metal, which is caused by the dried drop of sodium chloride solution. The samples in Fig. 5(a) and (b) had no acrylic coating and were exposed to high relative humidity (80%) at 25 °C and 35 °C, respectively. The corrosion pattern in Fig. 5(a) is highly compact and overall unremarkable; only its edge shows small-scale features that are reminiscent of dendritic patterns but might simply reflect random patterns created by the initial sandblasting of the surface. The structure in Fig. 5(b) shows filament-like traces that are characteristic of filiform corrosion. The traces are thin

and erratic compared to the more linear patterns in Fig. 5(c) and (d) and cover large portions of the surface at a rather high density.

The images in Fig. 5(c) and (d) show filiform corrosion under a thin (4.5  $\mu\text{m}$ ) and a thick (35  $\mu\text{m}$ ) acrylic coating, respectively. The experimental conditions are otherwise identical (Section 2) and at a slightly elevated temperature (38 °C). Filiforms forming under the thick film are wider than the ones under the thin film. Moreover, we find that the filiforms in Fig. 5(d) show fewer directional changes than those in Fig. 5(b) and (c). The image in Fig. 5(d) also shows several examples of closely spaced, parallel filaments that in some instances create the appearance of a single track of greater width.

The tendency of filiforms to hug or follow pre-existing corrosion tracks is further illustrated by the close-up images in Fig. 5(e)–(j), which also reveal details of filament collisions. The simplest form of collision occurs when an incoming filiform reflects off a pre-existing track, see Fig. 5(e)–(g). This most likely scenario should be distinguished from the rare cases in which both collision partners alter their direction (central part of Fig. 5(h)). An important question regarding the former case is the relation between the angle of incidence  $\theta_1$  and the angle of reflection  $\theta_2$ . This dependence is difficult to quantify owing to the non-zero width of travelling corrosion cells and the erratic variations of the pre-existing as well as the reflected filiform. Nonetheless, we observed numerous collision tracks that suggest the simple specular reflection law  $\theta_1 = \theta_2$  (see Fig. 5(e) and (f)). However, filiforms approaching the pre-existing track in a nearly perpendicular direction Fig. 5(g) tend to be more likely to trace the other track in the aforementioned hugging motion. This feature is obviously a strong deviation from a simple reflection law and is reminiscent of similar dynamics observed in the chemical garden system.<sup>16</sup>

Another important feature of filiform corrosion is the self-trapping of the travelling corrosion cells in their own or another cell's corrosion trails. This situation is shown in Fig. 5(i) and (j) and is likely to occur at a later stage for the sample in Fig. 5(h). Since the rust trails on steel essentially do not cross (the only

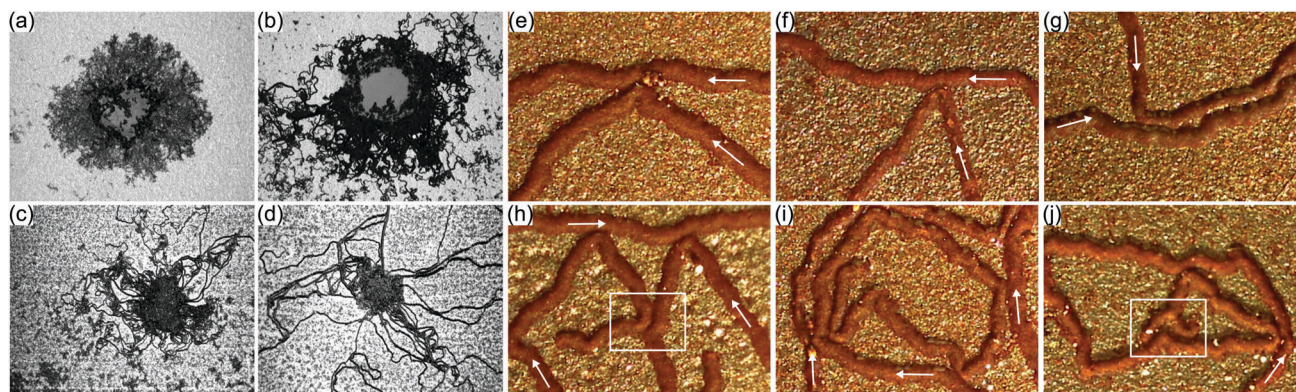


**Fig. 5** Corrosion patterns on low carbon steel. Samples (a and b) had no coating; samples (c and d) had thin (4.5  $\mu\text{m}$ ) and thick (35  $\mu\text{m}$ ) acrylic coatings, respectively. The reaction conditions in (a, b) and (c, d) exposed the samples to air and nitric acid vapour, respectively. Temperature: (a) 25 °C, (b) 35 °C and (c, d) 38 °C. Field of view in all frames:  $15.8 \times 11.8 \text{ mm}^2$ . (e–j) Zoom in view compared to (a–d) showing examples of filiform collisions on low carbon steel covered by an acrylic film (average thickness 35  $\mu\text{m}$ ). Note the self-entrapment in (i) and the rare splitting in (j). Arrows indicate the growth direction. Field of view:  $2.6 \times 2.0 \text{ mm}^2$ .

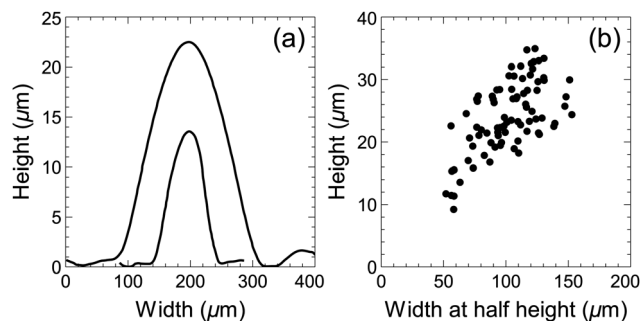


Fig. 6 Surface deformation caused by filiforms. (a) Two typical height profiles across the traces of filiform tracks obtained for film thicknesses of 4.5  $\mu\text{m}$  (lower curve) and 35  $\mu\text{m}$  (upper curve). (b) Maximal height of the tracks as function of their full width at half height.

exception known to us was documented in Fig. 5c of ref. 24), this trapping ultimately causes the extinction of the trapped corrosion cell owing to a lack of uncorroded, accessible surface area. On rare occasions one may also observe the splitting of corrosion cells, see Fig. 5(j). In the example shown, the splitting event was seemingly caused by the collision of the cell with a convex, highly curved segment of another filament.

Filiform corrosion is known to induce cathodic delamination, which is a pH-induced detachment of the coating from the metal substrate. This delamination, possibly in conjunction with other processes such as the formation of rust particles and osmosis, induces local height variations in the surface of the coating. We may characterize these changes by profilometric measurements along lines oriented perpendicular to and across the filament tracks. Two representative examples are shown in Fig. 6(a) and correspond to samples with film thicknesses of 4.5  $\mu\text{m}$  (low curve) and 35  $\mu\text{m}$  (upper curve). The profiles are bell-shaped curves that we analyse in terms of their height over the unperturbed surface and their full width at half height (Fig. 6(b)). The latter values are measured by fitting parabolae to the individual scanned profiles. The samples used for these measurements are exposed to the growth conditions for 42 days and cover a range of coating heights. The typical widths obtained by this method vary between 60 and 160  $\mu\text{m}$  and the corresponding heights are 10–35  $\mu\text{m}$ . Despite the noisy character of these measurements, one can conservatively approximate the dependence as proportional with a constant of proportionality around 1/5. However, for obvious physical reasons this dependence must saturate at a maximal height, which dictates a convex shape for the corresponding graph. We also note that the filiform widths measured by optical microscopy are very similar to the base widths of the filament profiles.

In the following we analyse the erratic directional changes of the travelling corrosion cell. The analyses are carried out for a set of 28 filiforms with an average width of

$$\langle W_T \rangle \pm \Delta W_T = (0.21 \pm 0.05) \text{ mm}, \quad (4)$$

measured from image analysis. In Fig. 7(a), the combined spectrum for all filiforms shows a broad distribution of wavenumbers up to approximately 4  $\text{mm}^{-1}$ , with a preferred value,

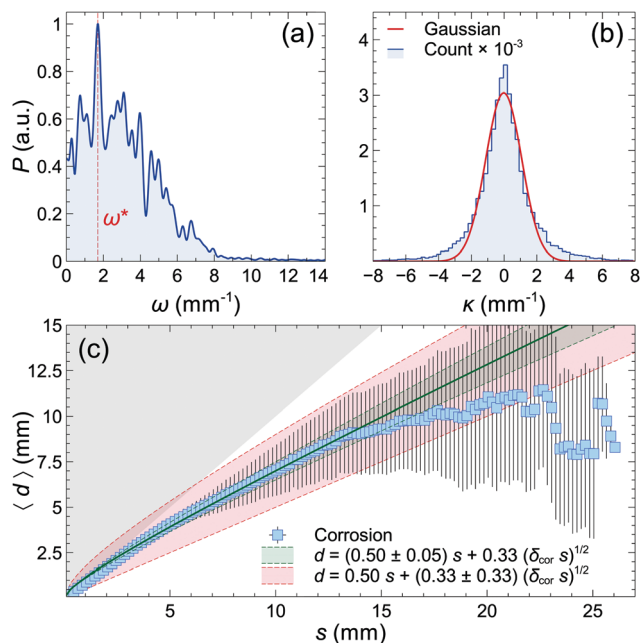


Fig. 7 Filiform corrosion: analysis of erratic directional changes along filiform trajectories. (a) Normalized power spectrum of the curvature data of 28 filiform trajectories. The preferred wavenumber,  $\omega^* = 1.7 \text{ mm}^{-1}$ , is also indicated. (b) Histogram of discrete values for the same data set together with a Gaussian fit. (c) Average Euclidean distance,  $\langle d \rangle$ , travelled by the 28 filiforms as a function of their arclength  $s$ . The shaded area indicates a forbidden region where  $d > s$ .

$\omega^*$ , around 1.7  $\text{mm}^{-1}$ , which is followed by a smooth decay at higher wavenumbers. Above approximately  $\omega_c \simeq 10 \text{ mm}^{-1}$  the power is essentially zero. The latter value is quite similar to the inverse average width of the filaments as explained above ( $\kappa_{\text{max}} \sim 2/((W_T) - \Delta W_T) \simeq 12.5 \text{ mm}^{-1}$ ). This finding implies that directional changes do not occur at length scales smaller than the width of the corrosion cell.

Fig. 7(b) shows the distribution of the curvature data in the form of a histogram where continuous values of the curvatures are grouped in discrete bins. As with chemical garden filaments, the shape of the histogram is essentially symmetric with respect to zero. The data can be well fitted by a Gaussian distribution, eqn (3), with  $\sigma = 1.1 \text{ mm}^{-1}$  and  $\kappa_0 = -0.02 \text{ mm}^{-1}$  ( $A = 3042$ ). The small value of  $\kappa_0$  confirms that, like the chemical garden filaments, the filiform motion does not break chiral symmetry.

Fig. 7(c) shows the plot of the average Euclidean distance,  $\langle d \rangle$ , measured from the starting point of the filament trail (near the nucleation zone) as a function of the filament arclength  $s$ . The method used to measure  $\langle d \rangle$  is the same as the one used for filaments, see Section 3. The relationship between  $d$  and  $s$  can be described by a scaling approach developed in Section 5.

## 5 Scaling and discussions

It is challenging to examine the behaviour of these two apparently distinct systems from a single theoretical argument. We do so by drawing an analogy between the dynamics of these systems and that of fluid flow in a porous medium.<sup>29</sup> As illustrated in Fig. 1

and 5, the tip of a filament has a random motion, during which its direction changes abruptly after short, relatively rectilinear flow paths. Fig. 4(a) and 7(a) show that a preferred length exists for such paths between abrupt turns. The typical distance between turns is estimated from  $\delta = 2\pi/(\omega^*)$ , where  $\omega^*$  is the preferred wavenumber, see Appendix B. Using the values of  $\omega^*$  obtained in Sections 3 and 4, we find  $\delta_{\text{cg}} = 15$  mm and  $\delta_{\text{cor}} = 3.7$  mm for chemical garden filaments and corrosion filiforms respectively.

The motion of the filaments may be described in terms of two components: the average speed of an ensemble of tips of the filaments,  $u$ , and a dispersive component associated with their random turns,  $D_e$ . We note that the dispersion in the position of the tips of the filaments occurs only in the presence of the advection of the tips, and hence  $D_e$  is a dispersion coefficient (*i.e.* rather than a diffusion coefficient). In these injection-driven chemical garden experiments, the speed is related to the flow rate of injection, and therefore an externally controlled variable, whereas for the filiform corrosion the filament speed is driven by osmosis, an internal chemical effect. In both cases, we expect the magnitude of the dispersive component to follow the scaling  $D_e \sim u\delta$ , where  $\delta$  is the typical distance between turns. This scaling can be obtained from a statistical analysis of the filament tip motion and is analogous to that for dispersion of a scalar during convection in a porous medium.<sup>29</sup> On the macro-scale, the radial position of the filament tips is therefore

$$d \simeq aut + b(D_e t)^{1/2} = as + b(D_e s/u)^{1/2} = as + b(\delta s)^{1/2}, \quad (5)$$

where  $a$  and  $b$  are constants and  $t$  is time. This relationship for  $d(s)$  comprises a term linear in  $s$  associated with the ballistic or advective motion and a sub-linear dispersive term,  $s^{1/2}$ , reflecting the random turns, and analogous to Brownian transport. We expect  $a \sim \cos\theta$ , where  $\theta$  is the nominal angle between the filament trajectories and the radial direction, and  $b$  of order 1. We show the predictions of this simple scaling for the chemical garden filaments and the filiform corrosion in Fig. 4(c) and 7(c), respectively. The theoretical predictions are in good agreement with the observations for both systems, taking  $\delta = 2\pi/(\omega^*)$ , and  $b = 0.33$ . We find  $a_{\text{cg}} = 0.45 \pm 0.05$  and  $a_{\text{cor}} = 0.50 \pm 0.05$ , corresponding to angles of  $63^\circ \pm 3^\circ$  and  $60^\circ \pm 3^\circ$  between the filament direction and the average direction of motion, for the chemical garden and corrosion experiments, respectively. The filiform corrosion shows a deviation from the theory at large  $s$  where self-trapping is present (see Fig. 5(h)–(j)), which reduces the exponent in  $s$ ; this effect is not considered in this model.

Rescaling both the Euclidean distance and the filament arclength by the preferred wavenumber,  $\bar{d} = d\omega^*$  and  $\bar{s} = s\omega^*$ , we obtain the following universal relationship

$$\bar{d} \simeq a\bar{s} + b(2\pi)^{1/2}\bar{s}^{1/2}. \quad (6)$$

This relation is satisfactorily compared with rescaled data for both chemical garden filaments and corrosion filiforms in Fig. 8 using  $a = (a_{\text{cg}} + a_{\text{cor}})/2 = 0.475 \pm 0.050$  ( $\theta \simeq 61.5^\circ \pm 3.0^\circ$ ) and  $b = 0.33 \pm 0.33$ .

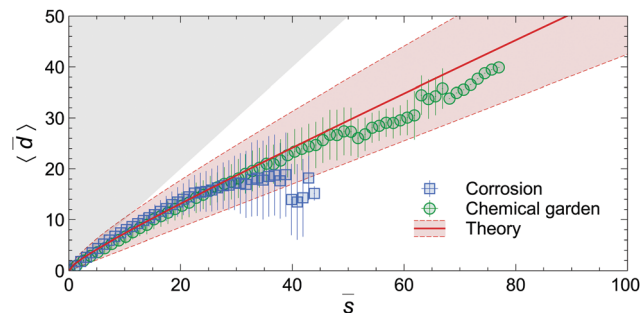


Fig. 8 Plot of the rescaled average Euclidean distance,  $\langle \bar{d} \rangle = \langle d \rangle \omega^*$ , travelled by all filaments/filiforms as a function of their rescaled arclength,  $\bar{s} = s\omega^*$ . The shaded area indicates a forbidden region (since  $\bar{d} \leq \bar{s}$ ).

It is interesting to note that although the evolution time for the filiform corrosion ( $\gtrsim 40$  days) is much larger than that for the chemical garden ( $\sim 15$  s), both systems exhibit similar geometry and dynamics. In the chemical garden, the relative ability of pressure associated with advection to break a precipitate cap in a filament and the chemical reaction to strengthen this cap is measured by the ratio of advective and transverse diffusive transport rates, the Péclet number,  $Pe = u_t \langle W_T \rangle / D$ , where  $\langle W_T \rangle$  is the average width,  $u_t = u/\cos\theta$  is the speed of the tips of the filaments and  $D$  the molecular diffusivity. We estimate  $Pe_{\text{cg}} = 10^4$  for an ion diffusivity  $D \sim 10^{-9} \text{ m}^2 \text{ s}^{-1}$  with  $u_t \approx 10^{-2} \text{ m s}^{-1}$  and  $W_T = 2.3 \times 10^{-3} \text{ m}$ . Such a large magnitude for  $Pe$  is responsible for the approximately rectilinear paths and the narrow width compared to length of the filaments. The analogous elongated geometry of corrosion filiforms suggests again a rapid longitudinal movement compared to slow transverse transport of ions; *i.e.*, large Péclet number. A hypothetical  $Pe_{\text{cor}} = 10^2$ – $10^4$  and a measured  $u_t \approx 10^{-8} \text{ m s}^{-1}$  together with  $\langle W_T \rangle = 2.1 \times 10^{-4} \text{ m}$  would indicate a rather low transverse diffusivity of  $D \sim 10^{-16}$ – $10^{-14} \text{ m}^2 \text{ s}^{-1}$ . This suggests that the growth of a corrosion filament is controlled by diffusion of ions in the solid surrounding the filiform. Such a mechanism explains the self-avoidance behaviour of the filiforms described earlier and seen in Fig. 5(e)–(j), as the metal is depleted of crucial ions in the area surrounding the filiform. We conclude then that, whether the flow is induced externally as in the injection-driven chemical garden or internally as in the corrosion filiforms, and whether the system evolves rapidly or slowly, the dynamics are similar owing to this chemical and physical balance.

## 6 Comparison and conclusions

Our study has revealed numerous similarities that had not been noted earlier between these different systems (Table 1). Chemical similarities include the product composition, basically a metal oxyhydroxide, that in the case of silicate chemical gardens typically also includes an outer layer of amorphous silica.<sup>30,31</sup> Earlier studies have analysed the detailed composition of the brown rust trail which typically contains a mixture of iron(II) and iron(III) hydroxides and oxides.<sup>19,32</sup> They both form filamentary reaction products at macroscopic length-scales and belong to the large

**Table 1** Comparison between filaments produced in chemical gardens confined to 2D and filiform corrosion

Feature	Filament	Filiform
Environment	Hele-Shaw cell	Liquid corrosion cell
Growth driving force	Injection	Osmosis
Average width (here)	2.3 mm	0.21 mm
Osmosis	Present	Dominant
Reactants	Metal salt solutions	
Reactant delivery	Through filament conduit	
Morphology	Fluid-filled filaments	
Reaction zone	Localized at filament tip	
'Hugging' motion	Yes	
Self-trapping	Observed	

class of self-organizing far-from-equilibrium systems. More specifically, the thread-like patterns arise from a localized reaction spot that travels through a quasi-two-dimensional system. In the case of filiform iron corrosion, this region is anodic and contains  $\text{Fe}^{2+}$  ions that form from the metal substrate and ultimately react with molecular oxygen that enters the reaction zone from the atmosphere. The steel surface can be compared to the reservoir of silicate solution in the Hele-Shaw cell in confined chemical gardens. The second reactant is delivered in confined chemical gardens through the conduit of the product trail. In filiform corrosion, for osmosis to be the driving force, then either the coating or the tail must be semipermeable. As we have discussed above, there are differing opinions as to whether or not the rust trail is an open channel. Either it is closed and reactants enter *via* the coating, as Slabaugh and Grotheer<sup>19</sup> suggest, or it is open and reactants enter that way, as in the chemical garden, as Ruggeri and Beck's<sup>20</sup> experiment indicates.

Inspection of Fig. 4 and 7 shows a difference of scale between chemical garden filaments and filiform corrosion mainly owing to the difference of preferred wavenumber (related to the difference of width) between these two structures in our experiments. On the other hand, in Fig. 8 the data of each filament/filiform have been rescaled by the preferred wavenumber  $\omega^*$ , where we may note how similar their dynamics are.

The silicate solution in the Hele-Shaw cell is a fluid medium in which privileged directions are found only as concentration gradients in the fluid. The directional changes observed in two-dimensional chemical gardens may be caused by the reaction product; likely candidates are small crystallites and other variations in the characteristics of the forming material. There may also be possible dynamical instabilities in tube growth. For filiform corrosion, imperfections of the steel surface, grain boundaries, and also spatial variations in the coating may be a major factor causing directional changes.

The variations from perfect ballistic motion observed in both systems imply that the product trails may collide with each other. These collisions are observed in both systems and can induce a hugging-type motion in which one filament follows the shape of a pre-existing one. In the corrosion case, we also observe collisions events that are reminiscent of specular reflection. Since in both experimental systems the motion of the reaction cell is fully self-avoiding, the erratic component in the motion also implies the possibility of the existence of self-trapping

events. Indeed, Fig. 4(b) and 7(b) show that the motion of these structures does not break the chiral symmetry whereas a local breaking of this symmetry is necessary for self-trapping since the filaments need to turn several times consecutively in the same direction, see Fig. 5(h)–(j). Self-trapping is thus expected to be a rare event except when self-avoiding filaments collide. These events are observed commonly in our corrosion experiments but are much less frequent for chemical gardens. Fig. 3(f) shows one of these rare events for chemical gardens. This difference results probably from a larger number of filiforms produced compared to chemical garden filaments, increasing thus the probability of collision. This difference in the number of structure produced is in turn due to a larger perimeter of the nucleation zone, compared to the width of the structure, for filiforms than for filaments.

Lastly, we reemphasize the fundamental role of osmosis in both systems, which for filiform corrosion has been noted as an integral part of the growth mechanism. While filament growth is driven instead by an external pump in the chemical garden experiments analysed here, osmosis nonetheless plays an important role in chemical gardens and is the essential mechanism that drives tube growth in classical chemical gardens that form around dissolving seed crystals. Thus, like chemical gardens, filiform corrosion is another example of a chemobronic system.<sup>9</sup>

## Conflicts of interest

There are no conflicts of interest to declare.

## Appendix

### A Power spectrum

Suppose that there are  $N$  data points  $\kappa_i \equiv \kappa(s_i)$ ,  $i = 1, \dots, N$  where the set of arclength  $s_i$  is unevenly spaced. In that case, the power spectrum (normalized periodogram) can be computed using the following expression<sup>33</sup>

$$P(\omega) = \frac{1}{2\sigma^2} \left\{ \frac{\left[ \sum_j (\kappa_i - \bar{\kappa}) \cos[\omega(s_i - S)] \right]^2}{\sum_j \cos^2[\omega(s_i - S)]} + \frac{\left[ \sum_j (\kappa_i - \bar{\kappa}) \sin[\omega(s_i - S)] \right]^2}{\sum_j \sin^2[\omega(s_i - S)]} \right\} \quad (7)$$

where the quantities  $\bar{\kappa}$ ,  $\sigma$  and  $S$  are given by

$$\bar{\kappa} = \frac{1}{N} \sum_{i=1}^N \kappa_i, \quad \sigma^2 = \frac{1}{N-1} \sum_{i=1}^N (\kappa_i - \bar{\kappa})^2, \quad (8)$$

$$\tan(2\omega S) = \frac{\sum_i \sin(2\omega s_i)}{\sum_i \cos(2\omega s_i)} \quad (9)$$

The constant  $S$  is a form of offset that makes  $P(\omega)$  independent of shifting all the  $s_i$ 's by any constant.

## B Typical length between turns

We give here additional information about how the typical distance between turns,  $\delta$ , is computed. For this purpose let us consider a simple hypothetical filament (or filiform) shown in Fig. 9(a). This structure is made of straight paths of length  $\ell$  and of turns with an average (here constant) curvature  $\kappa = 1/R$ . The total filament length  $L$  is given by  $L = n(\ell + 2\alpha R)$ , where  $n$  is the number of segments and the angle  $\alpha$  is defined in Fig. 9(a). The Euclidean distance travelled by the filament is  $d = n(\ell \cos \alpha + 2R \sin \alpha)$ . It is easy to see that  $d$  evolves linearly with the length of the filament.

The evolution of  $\kappa$  as a function of the arclength  $s$  is shown in Fig. 9(b). We get a ‘‘pulsating signal’’ with a spatial wavelength equals to  $\lambda_1 = \ell + 2\alpha R$  and the ‘‘duration of the pulse’’ is equal to  $\lambda_2 = 2\alpha R$ . The Fourier series of this signal is given by

$$\kappa(s) = a_0 + \sum_{k=1}^{\infty} a_k \cos(\omega_k s), \quad (10)$$

where

$$a_0 = \frac{2\alpha}{2\alpha R + \ell}, \quad a_k = \frac{2}{k\pi R} \sin\left(\frac{k\pi\lambda_2}{\lambda_1}\right), \quad (11)$$

$$\omega_k = \frac{2\pi k}{\ell + 2\alpha R}. \quad (12)$$

We notice that  $a_1$  has the largest magnitude ( $a_0$  is just a shift). Therefore, the preferred wavenumber is

$$\omega^* = \omega_1 = \frac{2\pi}{\ell + 2\alpha R}. \quad (13)$$

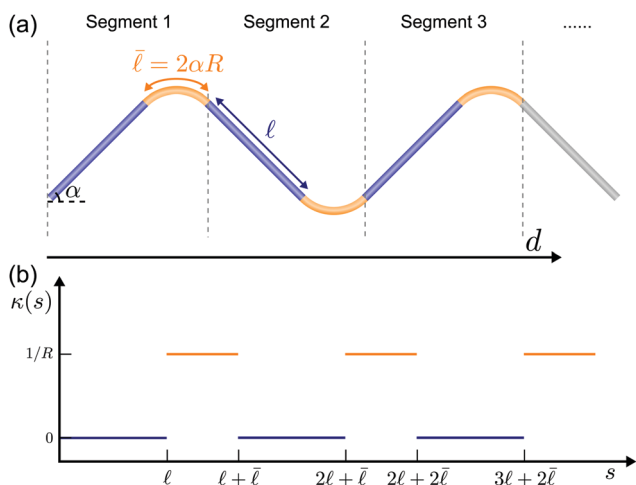


Fig. 9 (a) Schematic of an hypothetical filament or filiform. (b) Corresponding curvature  $\kappa$  as a function of the arclength  $s$ .

Defining  $\delta = 2\pi/\omega^*$ , we have

$$\delta = \ell + 2\alpha R. \quad (14)$$

For filaments and filiforms, we typically have  $\ell \gg R$  such that  $\delta \simeq \ell$  is the typical distance between turns. Indeed, in Fig. 3(c), we notice that the turns with the largest curvatures (the most significant turns) are characterized by  $\kappa \sim 1 \text{ mm}^{-1}$ , and thus  $R \sim 1 \text{ mm}$ , whereas the curvilinear distance ( $\ell = \Delta s$ ) between those turns is at least 5 mm ( $\ell \gg R$ ). For filiforms, Fig. 5 clearly shows that the typical distance between turns  $\ell$  is also much larger than the radius of curvature  $R$  of these turns such that  $\delta \sim \ell$ .

## Acknowledgements

O. S.'s work was supported by the US National Science Foundation under grant no. 1609495. A. D., F. H., and F. B. acknowledge the Belgian PRODEX for financial support. S. S. S. C. acknowledges the financial support of the UK Leverhulme Trust project RPG-2015-002. J. H. E. C. acknowledges the financial support of the Spanish MINCINN project FIS2016-77692-C2-2-P. We thank V. Brasiliense for performing some experiments on confined chemical gardens.

## References

- 1 G. Nicolis and I. Prigogine, *Self-organization in non-equilibrium systems*, Wiley, New York, 1977.
- 2 J. A. Pojman and I. R. Epstein, *An Introduction to Nonlinear Chemical Dynamics: Oscillations, Waves, Patterns, and Chaos*, Oxford University Press, Oxford, 1998.
- 3 E. Nakouzi and O. Steinbock, *Sci. Adv.*, 2016, **2**, e1601144.
- 4 R. S. Lillie, *J. Gen. Physiol.*, 1925, **7**, 473–507.
- 5 K. Agladze and O. Steinbock, *J. Phys. Chem. A*, 2000, **104**, 9816–9819.
- 6 C. Punckt, M. Bölscher, H. H. Rotermund, A. S. Mikhailov, L. Organ, N. Budiansky, J. R. Scully and J. L. Hudson, *Science*, 2004, **305**, 1133–1136.
- 7 J. Christoph and M. Eiswirth, *Chaos*, 2002, **12**, 215–230.
- 8 R. D. Coatman, N. L. Thomas and D. D. Double, *J. Mater. Sci.*, 1980, **15**, 2017–2026.
- 9 L. M. Barge, S. S. S. Cardoso, J. H. E. Cartwright, G. J. T. Cooper, L. Cronin, A. De Wit, I. J. Doloboff, B. Escibano, R. E. Goldstein, F. Haudin, D. E. H. Jones, A. L. Mackay, J. Maselko, J. J. Pagano, J. Pantaleone, M. J. Russell, C. I. Sainz-Daz, O. Steinbock, D. A. Stone, Y. Tanimoto and N. L. Thomas, *Chem. Rev.*, 2015, **115**, 8652–8703.
- 10 S. Thouvenel-Romans and O. Steinbock, *J. Am. Chem. Soc.*, 2003, **125**, 4338–4341.
- 11 D. A. Stone and R. E. Goldstein, *Proc. Natl. Acad. Sci. U. S. A.*, 2004, **101**, 11537–11541.
- 12 J. Pantaleone, A. Tóth, D. Horváth, J. R. McMahan, R. Smith, D. Butki, J. Braden, E. Mathews, H. Geri and J. Maselko, *Phys. Rev. E: Stat., Nonlinear, Soft Matter Phys.*, 2008, **77**, 046207.

- 13 J. Pantaleone, A. Tóth, D. Horváth, L. RoseFigura and J. Maselko, *Phys. Rev. E: Stat., Nonlinear, Soft Matter Phys.*, 2009, **79**, 056221.
- 14 F. Haudin, J. H. E. Cartwright, F. Brau and A. De Wit, *Proc. Natl. Acad. Sci. U. S. A.*, 2014, **111**, 17363–17367.
- 15 F. Haudin, V. Brasiliense, J. H. E. Cartwright, F. Brau and A. De Wit, *Phys. Chem. Chem. Phys.*, 2015, **17**, 12804.
- 16 F. Haudin, J. H. E. Cartwright and A. De Wit, *J. Phys. Chem. C*, 2015, **119**, 15067–15076.
- 17 W. Funke, *Prog. Org. Coat.*, 1981, **9**, 29–46.
- 18 M. G. Fontana and N. D. Greene, *Corrosion engineering*, McGraw-Hill, New York, 1967.
- 19 W. H. Slabaugh and M. Grotheer, *Ind. Eng. Chem.*, 1954, **46**, 1014–1016.
- 20 R. T. Ruggeri and T. R. Beck, *Corrosion*, 1983, **39**, 452–465.
- 21 M. A. Hill, R. K. Schulze, J. F. Bingert, R. D. Field, R. J. McCabe and P. A. Papin, *J. Nucl. Mater.*, 2013, **442**, 106–115.
- 22 G. M. Hoch, *Localized corrosion*, Houston, 1974, pp. 134–142.
- 23 C. F. Sharman, *Nature*, 1944, **153**, 621–622.
- 24 H. Kaesche, *Werkst. Korros.*, 1959, **11**, 668–681.
- 25 R. S. J. Preston and B. Sanyal, *J. Appl. Chem.*, 1956, **6**, 26–44.
- 26 J.-L. Delplancke, S. Berger, X. Lefèbvre, D. Maetens, A. Pourbaix and N. Heymans, *Prog. Org. Coat.*, 2001, **43**, 64–74.
- 27 M. Van Loo, D. D. Laiderman and R. R. Bruhn, *Corrosion*, 1953, **9**, 277–283.
- 28 M. Morcillo, F. J. Rodríguez and J. M. Bastidas, *Prog. Org. Coat.*, 1997, **31**, 245–253.
- 29 O. M. Phillips, *Flow and Reactions in Permeable Rocks*, Cambridge University Press, 1991.
- 30 J. J. Pagano, S. Thouvenel-Romans and O. Steinbock, *Phys. Chem. Chem. Phys.*, 2007, **9**, 110–116.
- 31 J. H. E. Cartwright, B. Escibano and C. I. Sainz-Díaz, *Langmuir*, 2011, **27**, 3286–3293.
- 32 J. Weissenrieder and C. Leygraf, *J. Electrochem. Soc.*, 2004, **151**, B165–B171.
- 33 N. R. Lomb, *Astrophys. Space Sci.*, 1976, **39**, 447–462.